Elastic properties of ferropericlase at lower mantle conditions and its relevance to ULVZs

Joshua M.R. Muir*, John P. Brodholt

Department of Earth Sciences, University College London, Gower Street, London WC1E 6BT, UK

A B S T R A C T

The elasticity of $Fe_xMg_{1-x}O$ was examined under lowermost mantle temperature and pressure conditions using density functional theory (DFT). The addition of iron decreases the shear modulus of MgO but has varying effects on the bulk modulus depending on the spin state of the iron. The spin state of iron in $Fe_xMg_{1-x}O$ is dependent on pressure and temperature but also on the concentration of iron. At 136 GPa, Fe in low concentrations ($<25\%$) is nearly entirely low spin, while at very high concentrations ($>75\%$) it is nearly entirely in the high spin state. There is, as expected, a large decrease in seismic velocities with iron substitution. However, the effect of Fe is greater at high-temperatures than at low-temperatures, meaning it is difficult to extrapolate low-temperature experimental results. We cannot simultaneously match the density and seismic velocities of ULVZs with Fe-enriched ferropericlase. This is reflected in $(d\ln V_s/d\ln V_p)_{T,P}$, which in ULVZs is generally observed to be about 3, but does not exceed about 1.5 for Fe-enriched periclase. A mixture of ferropericlase and ferrous perovskite can cause V_s decreases of up to 45%, which allows the range of ULVZ V_p, V_s and densities to be matched. We also find that $(d\ln V_s/d\ln V_p)_{T,P}$ increases up to as much as 3 but this value is strongly dependent on the bounds of the mixing geometry. We conclude, therefore, that the properties of ULVZs can be readily explained by a lower mantle with a single phase that is heavily enriched in Fe.

© 2015 The Authors. Published by Elsevier B.V. This is an open access article under the CC BY license (http://creativecommons.org/licenses/by/4.0/).

1. Introduction

Ultra-Low Velocity Zones (ULVZ) are small regions in the lowermost mantle with much lower velocity and higher density than the surrounding mantle ($\Delta\rho$ 5–15%, ΔV_p 8–15%, ΔV_s 24–45%) (Jensen et al., 2013; Rondenay et al., 2010; Thorne et al., 2013). A defining value of ULVZs is that $(d\ln V_s/d\ln V_p)_{T,P}$ is observed to be about 3 (Thorne et al., 2013), although values closer to 2 have also been speculated (Hutko et al., 2009; Idehara et al., 2007). There are two common explanations for ULVZs; one is that they are areas of partial melt (Hernlund and Jellinek, 2010; Nomura et al., 2011) and the other is that they are enriched in iron (Bower et al., 2011; Dobson and Brodholt, 2005; Mao et al., 2006). The latter could arise as the final product of crystallisation of a deep magma ocean (Labrosse et al., 2007; Nomura et al., 2011; Thomas et al., 2012), the incorporation of some iron from the core (Buffett et al., 2000; Garnero and Jeanloz, 2000; Kanda and Stevenson, 2006; Manga and Jeanloz, 1996; Mao et al., 2006; Petford et al., 2005), or from ultra-

dense remains of past subduction (Dobson and Brodholt, 2005). Both partial melts and iron-enrichment can strongly decrease seismic velocities, but whether either is able to simultaneously match the observed P and S anomalies, and the observation of about 10% increase in density in ULVZs, is not yet clear.

The incorporation of iron acts to strongly increase the density and reduce the velocities of the host phase, be it perovskite (bridgmanite) (pv), ferro-periclase (fp) or a melt. To first order the density is increased and velocities reduced simply due to the inherent high density of the iron atom relative to magnesium (Mg), but the exact details depend on how Fe affects the bulk and shear modulus. In a recent study (Muir and Brodholt, 2015), we used *ab initio* methods to show that the incorporation of large amounts of ferrous iron into pv is unlikely to produce the reductions in V_p and V_s and increases in density observed in ULVZs. This is because V_p and V_s decrease by roughly similar amounts with Fe. Most of the recent observations of ULVZs give a value for $(d\ln V_s/d\ln V_p)_{T,P}$ of about 3, while most experimental and theoretical studies of Fe-enriched phases predict lower values of between 1 and 2 (Dorfman and Duffy, 2014; Scanavino and Prencipe, 2013; Sinmyo et al., 2014; Stackhouse et al., 2007).

However, a recent study Wicks et al. (2010) concluded that iron-enriched fp rather than iron-enriched pv may be able to match ULVZ properties. This is based on their experiments at high-pressure which showed that iron affected the velocities of fp much more than expected. When making corrections for temperature, Wicks et al. (2010) found that V_p, V_s and density of ULVZs could all be matched with ∼84% iron Fe enrichment in the fp when mixed with 88% vol percent pv. These experiments, however, were performed at room temperature and, as we show here, temperature has a number of important effects; not only will it decrease the bulk and shear moduli but it also changes the proportion of high and low spin Fe which further affects the elasticity of ferropericlase.

There have been a number of other studies attempting to characterise the effect of large concentrations of iron in fp. For instance, the variation in the bulk modulus (K) of fp with Fe content (dK/dFe) has been surveyed for a wide range of studies (Scanavino and Prencipe, 2013). Theoretical results under ambient conditions and for Fe concentrations less than about 50% (Scanavino and Prencipe, 2013; Wu et al., 2013) show an increase of ∼0.1 (GPa/Fe%) in K and a similar decrease in the shear modulus (G). They also found that the effect of Fe on the moduli increased with increasing pressure. For more strongly enriched iron concentrations there is a negligible difference in K compared to MgO (Isaak and Moser, 2013), but a possible large decrease in G (Lu et al., 2005; Scanavino et al., 2012). The increase in density associated with the incorporation of iron causes large decreases in seismic velocities, with dV_s/dFe ∼−0.03 km s^{-1}/%Fe and dV_p/dFe ∼−0.04 km s^{-1}/%Fe at ambient conditions (Chen et al., 2012; Jacobsen et al., 2002; Reichmann et al., 2000; Sinmyo et al., 2014; Wicks et al., 2010; Wu et al., 2013). Again, increased pressure seems to increase the magnitude of these derivatives slightly (Sinmyo et al., 2014).

To complicate matters, fp undergoes a spin transition from high spin ($S = 2$) to low spin ($S = 0$) with increasing pressure. Intermediate spin states are only metastable and thus should not be overwhelmingly present (Larico et al., 2013). For low amounts of iron (<20%) the spin transition is concentration independent, occurring between 40–60 GPa at ambient temperatures and rising to 70–125 GPa for mid-mantle temperatures (2200–2400 K) (Lin et al., 2013). Larger concentrations of iron act to increase spin transition pressures (Lin et al., 2007a; Persson et al., 2006; Speziale et al., 2005). Temperature acts to broaden the spin-crossover region and moves it to higher pressures, and this region can be theoretically treated as an ideal mixture of low and high spin states (Lin et al., 2007b; Wentzcovitch et al., 2009; Wu et al., 2009, 2013). The low spin state has a density 1–5% larger than the high spin state and a K that is 1–4% larger (Lin et al., 2013; Wu et al., 2013). Within the spin-transition region K and V_p decrease by as much 50%, but this becomes less pronounced and more spread out with temperature (Lin et al., 2013; Wentzcovitch et al., 2009; Wu et al., 2013; Wu and Wentzcovitch, 2014). G and ρ remain essentially unaffected by the spin transition.

In this paper we examined the full range of iron substitution from MgO to FeO at the pressure and temperature of the base of the mantle. In this way we can elucidate how well low pressure and low temperature trends hold up in predicting lower mantle properties.

2. Methods

All simulations were carried out with the DFT code VASP (Kresse and Furthmuller, 1996) using the projector-augmented-wave (PAW) method (Kresse and Joubert, 1999) and the PBE formulation of GGA corrected for solids (Perdew et al., 2008). The core radii of the PAW spheres are O 0.80 Å ($2s^2 2p^4$), Mg 1.06 Å

($2p^6 3s^2$), Fe 1.22 Å ($3d^7 4s^1$). 14 electron Fe potentials were also tested and the results are similar. Hubbard U parameters were set to 3 eV.

For $Mg_x Fe_{1-x}O$ we studied the elasticity of structures with $x =$ 0, 0.25, 0.5, 0.75 and 1. For intermediate iron concentrations, iron atoms were placed at maximum separation which was found to be the most stable configuration at 0 K and 136 GPa. Alternate arrangements of iron were tested and were found to be less stable and with increases in V_p of <614 m/s and V_s < 232 m/s.

Both static and high temperature molecular dynamics (MD) runs were performed. All runs were performed with a cubic 64 atom unit cell ($2a * 2b * 2c$). Static runs were calculated at $4 \times 4 \times 4$ k points and MD runs were calculated at the gamma point. To ensure k point sufficiency we tested larger k point meshes for both unstrained and strained unit cells and found no significant difference in output stresses or in atom vibrations for dynamic runs. Static runs had an energy cutoff of 850 eV and self-consistent runs were relaxed to within 10^{-6} eV. MD runs had cutoffs of 650 eV and 10^{-4} eV. MD trajectories were performed in the *NVT* ensemble using the Nosé thermostat (Nose, 1984) for 6–10 ps (10 ps for undeformed states, 6 ps for strained states). Nosé frequencies were ∼20 THz.

Isothermal elastic constants were calculated by applying four strain magnitudes (±0.02 and ±0.01) to one axial and one triclinic strain. The calculation of adiabatic elastic constants and uncertainties is the same as in Muir and Brodholt (2015). To calculate properties of ferropericlase with Fe in the high spin state we fixed the overall spin to the ferromagnetic value, and for low spin states we used a non-spin polarised calculation. We also ran some spin-polarised simulations without fixing of any spin states. These are not likely to represent the true spin-state of fp at those P and T conditions since the runs do not include the magnetic or vibrational entropy within the electronic inner loop, but they do provide information on the properties of fp with that particular set of spins. All reported ferropericlase results are on B1 structures, the free energy of IB8 and NB8 hexagonal structures was calculated and at the lower mantle conditions of 136 GPa and 2000–4000 K the B1 structure was more stable for all iron concentrations.

For all systems studied elasticities were calculated at 136 GPa and 2000 K, 3000 K, 4000 K and static conditions for high, low and unfixed spin systems. Spin transition enthalpies were calculated in static conditions at 0, 30, 60, 90, 136 and 150 GPa. The entropy of spin transition was calculated at 60, 90, 136 and 150 GPa and 2000 and 4000 K.

In order to calculate the concentration of high and low spin iron under any P&T condition, we used:

$$n_{LS}(P, T) = \frac{1}{1 + \exp(\frac{\Delta G_{LS-HS}}{n_{Fe} K b T})} \quad (1)$$

where n_{LS} is the proportion of states in the low spin state, ΔG is the free energy difference (including magnetic, vibrational and electronic entropy) between a unit cell of low spin and high spin fp and n_{Fe} is the number of iron atoms per unit cell (Wentzcovitch et al., 2009). Electronic entropy is determined directly from VASP. The vibrational entropy is determined using thermodynamic integration with the blue-moon algorithm in VASP (Bucko, 2008) along 5 image paths and with constraints placed on the Fe–O and Fe–Fe bond lengths of a random iron. Magnetic entropy was determined using Eq. (2):

$$S_{mag} = \ln(\mu + 1) \times R \times n_{Fe} \quad (2)$$

where R is the gas constant and μ is the average absolute magnetic moment of an individual iron atom determined from VASP. Note that this does not contain a term for magnetic degeneracy

Table 1

Spin transition pressure as a function of iron content ($Fe_xMg_{1-x}O$) (in GPa) at 0 K and entropy and Clasius–Clapeyron slopes of FeO at 4000 K. Lower iron concentrations had proportionality lower entropies but also proportionally smaller spin transition volume changes and so the Clausius–Clapeyron slope was independent of iron concentration. The data from Speziale et al. (2005) are from Mössbauer spectroscopy at 10 K and have errors of 10 GPa.

	Spin transition (GPa)			S_{mag} (meV/KFe$_{atom}$)	S_{vib} (meV/KFe$_{atom}$)	S_{elec} (meV/KFe$_{atom}$)	$-\Delta S/\Delta V$ (GPa/K)
Iron content	$X = 0.25$	0.5	1	1	1	1	1
Speziale et al. (2005)	44	60	92				
$Fe_xMg_{1-x}O$	34	66	93	−0.12	−0.015	−0.0075	0.016

since that is already contained in the electronic entropy. To convert from magnetic moment to spin (S_a) we used a conversion factor determined by setting a 0 GPa FeO structure ($\mu = 3.70$ per iron) to $S = 2$.

Following Wentzcovitch et al. (2009) the volume of the mixed spin unit cell is determined by Eq. (3):

$$V(n) = n_{LS}V_{LS}(P,T) + (1 - n_{LS})V_{HS}(P,T) \qquad (3)$$

where V is the volume of the various spin states. The moduli at any particular temperature are then determined by Eq. (4):

$$\frac{V(n)}{K(n)} = n\frac{V_{LS}}{K_{LS}} + (1 - n)\frac{V_{HS}}{K_{HS}} - (V_{LS} - V_{HS})\frac{\partial n_{LS}}{\partial P}\bigg|_T \qquad (4)$$

(Wu and Wentzcovitch, 2014). A similar expression is used for G, but in this case the final term is 0.

The moduli of single phase systems were determined via the Reuss (R), Voigt (V) and Voigt–Reuss–Hill (VRH) averaging schemes. The elastic properties of the polyphase systems were obtained using the Hashin–Shtrikman bounding method (HS) (Davies, 1974).

3. Results

3.1. Spin states

Table 1 lists the spin transition pressure of $Fe_xMg_{1-x}O$ structures at 0 K and their Clausius–Clapeyron slopes. At 0 K the enthalpy change of the spin transition is quite small and so at 136 GPa, FeO is most stable in a random mixed spin state with n_{LS} of 0.2. At elevated temperature all spins are found to be paramagnetic. A large increase in magnetic entropy (and somewhat the vibrational entropy) stabilises the high spin state at high temperature and increases the spin transition pressure. The average spin of each iron atom decreases with temperature from $S = 1.82$ at 0 K to 1.43 in pure FeO at 4000 K. In $Fe_{0.5}Mg_{0.5}O$ the average spin becomes 1.28. These values are between a high ($S = 2$) and an intermediate spin ($S = 1$). No distortion in iron sites was seen upon heating and thus this decrease is likely due to thermal broadening effects, rather than a true intermediate state.

To calculate the effect of temperature on the proportion of high and low spins, we treated a mixture of them as an ideal-solid solution using Eq. (1). The results are shown in Fig. 1. For low iron concentrations (<25%) we find that iron should be almost entirely low spin in the very deepest mantle (136 GPa) at all temperatures, with only a slight decrease in n_{LS} to 0.98 at 4000 K. A slightly larger decrease in n_{LS} of 0.1–0.2 between 3000 and 4000 K for these iron concentrations has been seen theoretically in other studies due to the difference in QHA and thermodynamic integration methods (Fukui et al., 2012; Wentzcovitch et al., 2009; Wu et al., 2009). At higher concentrations of iron, temperature affects the proportion of low spin to high spin more. For completeness it is worth pointing out that unfixed spin calculations predict $Fe_{0.25}Mg_{0.75}O$ to be entirely low spin up to 4000 K and $Fe_{0.5}Mg_{0.5}O$, $Fe_{0.75}Mg_{0.25}O$ and FeO to be entirely high spin up to 4000 K.
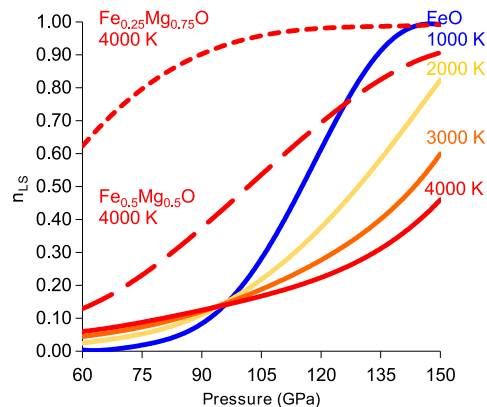

Fig. 1. Proportion of iron in the low spin state (n_{LS}) as a function of pressure and temperature for FeO (solid lines). $Fe_{0.25}Mg_{0.75}O$ and $Fe_{0.5}Mg_{0.5}O$ at 4000 K are also shown as dotted and dashed lines respectively.
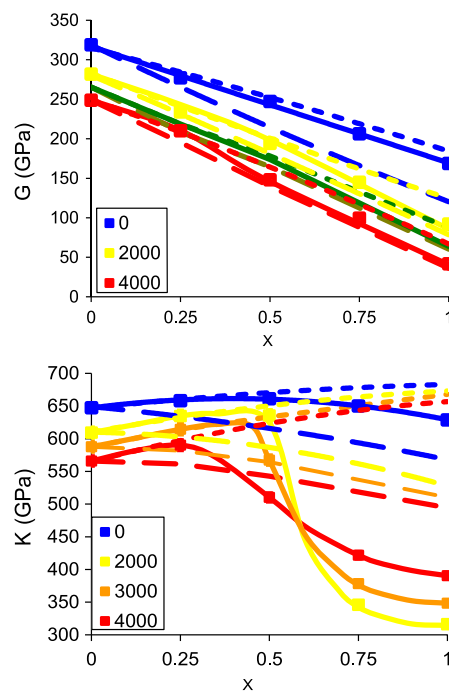

Fig. 2. Graph of VRH shear and bulk modulus (adiabatic) of $Fe_xMg_{1-x}O$ as a function of iron concentration, temperature and spin (dashed lines = high spin, dotted line = low spin, solid lines = spin corrected) at 136 GPa. Spin correction cannot be performed at 0 K so the spin correction is simply a spin unfixed run. Values at $x = 0$, 0.25, 0.5, 0.75 and 1 were computed by VASP and trends in K, G, enthalpy, entropy, n_{LS} and dn_{LS}/dp were then calculated from these values for intermediate iron concentrations using equations given in the text. Statistical error is <1.5% for all thermal samples.

3.2. Elasticity

The elasticity of $Fe_{xx}Mg_{1-x}O$ is shown in Figs. 2–5 and selected values are tabulated in Table 2.

Table 2

Bulk and shear moduli (VRH averaged) for high spin (HS) and low spin (LS) states for various iron concentrations and the derivatives of the moduli with iron concentration at 136 GPa. Results given are at 0 and 4000 K. In the derivatives, X represents either K or G. The statistical error for 4000 K results is calculated to be <1.5%.

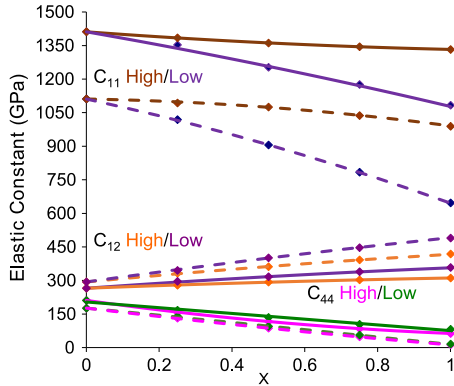| | K (adiabatic) | | | | G | | | |
| | 0 K | | 4000 K | | 0 K | | 4000 K | |
	HS	LS	HS	LS	HS	LS	HS	LS
MgO (GPa)	647	647	566	566	319	319	249	249
$Fe_{0.25}Mg_{0.75}O$	638	659	561	594	265	274	195	210
$Fe_{0.5}Mg_{0.5}O$	613	672	543	626	215	260	140	163
$Fe_{0.75}Mg0.25O$	594	678	523	643	168	218	88	109
FeO	568	683	494	656	120	183	36	67
dX/dFe (GPa/K)	−0.82	0.35	−0.75	0.90	−1.98	−1.31	−2.13	−1.84
dX/dT (FeO)			−0.019	−0.010			−0.021	−0.029
dX/dT (MgO)			−0.020	−0.020			−0.018	−0.018

Fig. 3. The variation in adiabatic elastic constants of $Fe_{xx}Mg_{1−x}O$ with varying iron content for high- and low-spin states at 0 K (solid lines) and 4000 K (dashed lines) and 136 GPa. The statistical error for each constant at 4000 K is <1.5%.

Firstly we examine the effect of iron on the elasticity of the end-member high and low spin states. At 0 GPa we find that iron has a negligible or very small effect on both the bulk and shear moduli (dK/dFe% = 0 and dG/dFe% = −0.16), but at 136 GPa iron has a far more significant effect on the moduli which is dependent on the iron spin state and the temperature (Table 2). As expected, G decreases with iron content and with temperature, regardless of the spin state. Interestingly, K decreases with iron content for the high spin state, but increases with iron content for the low spin state. At a fixed spin state temperature decreases K as expected but since temperature also affects the proportion of high-low spin, the real effect of temperature on K shows some interesting behaviour, as discussed below. The variable modulus changes seen in some experiments (Scanavino and Prencipe, 2013) could thus be reflective of differing iron spin states. The elasticity of calculations with no spin fixing (spin unfixed) are virtually identical to those of the relevant spin fixed sample.

The effect of spin state on K at 136 GPa is reflected in the individual elastic constants (Fig. 3). The addition of iron decreases C11 and C44 but increases C12. dG/dFe is larger for high spin iron because C44 is affected more by high spin iron than by low spin iron. dK/dFe is negative for high spin iron since C11 is more affected than C12 by high spin iron whereas the opposite occurs for low spin iron leading to a positive dK/dFe. These effects may be explained by the arrangement of the d-electrons between the Fe–O bonds. Octahedral crystal field splitting predicts the higher energy e_g orbitals (d_{z2} and $d_{x2−y2}$) to lie along the Fe–O bonds and the lower energy t_{2g} orbitals (d_{xy}, d_{zx} and d_{zy}) to lie between them. High spin iron should have more electrons in e_g orbitals than low spin iron and thus should resist Fe–O bond shortening and, therefore, compression more than low spin iron. It's not quite so obvious whether an analogous explanation can be used to understand why low-spin Fe resists shear more than high-spin Fe.

We then obtained the elasticity for mixed spin state (Mg, Fe)O using the spin values in Fig. 1 and Eq. (3). This requires us to find dn_{LS}/dP, which we obtained by calculating n_{LS} at each temperature for 60, 90, 136 and 150 GPa, fitting to a second-order polynomial and then taking the pressure derivative. As can be seen in Fig. 2, the bulk moduli for the mixed spin-states are very different from that of the end member high- and low-spin states, and become particularly pronounced at high concentrations of Fe. For instance in FeO at 2000 K, the bulk modulus is about half that of the average of the high- and low-spin states. This can be understood by considering the slopes of n_{LS} as a function of pressure and temperature in Fig. 1. The proportion of high to low spin states is not changed by shear strain (Wu and Wentzcovitch, 2014) and so G merely represents an average of the high and low spin values.

The elastic anisotropy was also examined (Fig. 4). FeO and MgO have a similar pattern of anisotropy at 0 and 4000 K, with only a slight increase in absolute anisotropy in FeO. Low spin iron has higher absolute anisotropy than high spin iron.

Fig. 5 plots (Mg, Fe)O velocities as function of density for three different temperatures at 136 GPa. The density at a particular temperature is, therefore, controlled entirely by the concentration of Fe and its spin state. As expected, velocities decrease considerably with iron concentration due to the increased density of the Fe iron relative to Mg, and due to the softening of K and G. V_s decreases reasonably smoothly with density, whereas V_p shows a more complicated pattern, reflecting the strong effect of K on pressure as shown in Fig. 2.

Fig. 5 shows the VRH average of velocity as well as the V and R bounds. At high temperatures (4000 K) the shear modulus of FeO is only 1/5 that of MgO (Fig. 2) and thus small differences in G (<20 GPa) due to different averaging schemes causes large differences in the V_s. Nevertheless, even the lowest bound (Reuss) V_s is still too high for ULVZs.

At 0 GPa our calculated velocities match pure FeO (Isaak and Moser, 2013) and MgO experimental values (Kono et al., 2010), while our velocities as a function of iron content match the experimental slopes found in Jacobsen et al. (2002). At this pressure the VRH, R and V bounds are all similar enough to fit the experimental data. At 136 GPa our results do not compare to those of highly enriched iron found in Wicks et al. (2010). At 0 GPa and 0 K and 85% Fe, we obtain V_p and V_s of 6.6 and 2.6 km/s respectively, which compare well with ambient condition V_p and V_s of 6.8 and 2.8 km/s of Wicks et al. (2010). At 136 GPa and 300 K, however, we obtain V_p of 10.1 and V_s of 4.8 km/s compared to a V_p of 7.5 and a V_s of 3.8 for Wicks et al. (2010). It is unclear why there is so much difference between our results and the high-pressure velocities of Wicks et al. (2010). We note, however, that the velocities of Wicks et al. (2010) seem to be remarkably insensitive to pressure, in particular V_p which only increase from 6.8 to 7.5 km/s over a pressure range of 136 GPa which may be due to the transition to a hexagonal structure above ∼80 GPa which would not
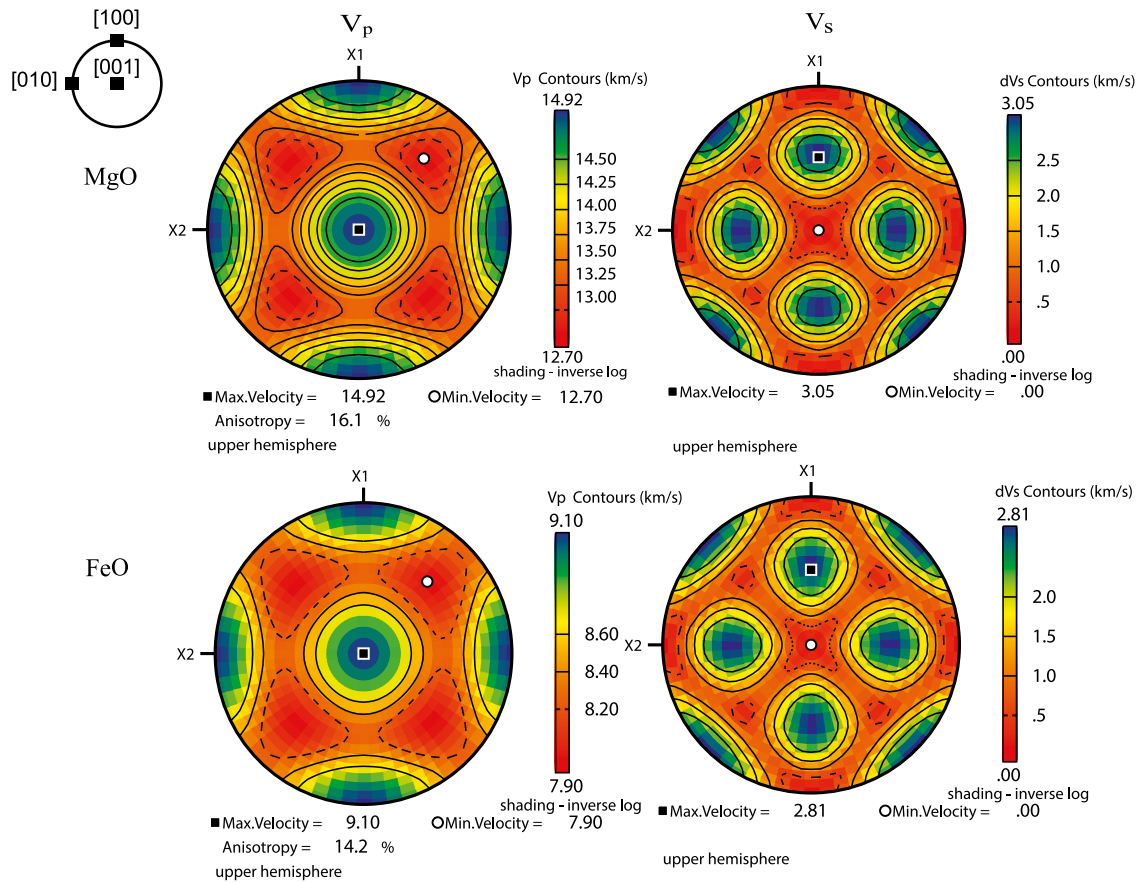
Fig. 4. Anistropy of 4000 K and 136 GPa FeO (spin unfixed) and MgO structures. The anisotropy is remarkably similar between the two compositions. V_p diagrams show the V_p speed in every direction whereas V_s diagrams show the shear wave splitting (V_{s1}–V_{s2} dV_s) in every direction.
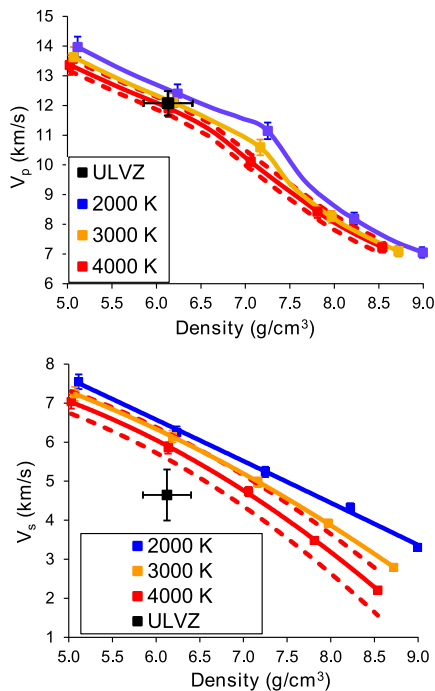

Fig. 5. V_p and V_s of $Fe_xMg_{1-x}O$ as a function of density (by varying iron) at 2000 K, 3000 K and 4000 K and at 136 GPa. The moduli were calculated at $x = 0$, 0.25, 0.5, 0.75 and 1 and then interpolated between these points as in Fig. 2. Black squares are the expected ULVZ values ($\Delta\rho$ 5–15%, ΔV_s 8–16%, ΔV_p 25–45% from PREM). Solid lines are VRH averages, red dotted lines are the V and R bounds at 4000 K. Error bars are statistical errors which are <1.5%. (For interpretation of the references to color in this figure legend, the reader is referred to the web version of this article.)

be stable at lower mantle temperatures (Ozawa et al., 2010). It has also been observed that NIS measurements of sound velocities on solid solutions differ from those measured with ultra-sonic methods (Sinmyo et al., 2014). This leads to the suggestion that the NIS sound-velocity measurements of Wicks et al. (2010) may be affected by the element-specific nature of the NIS technique (Sinmyo et al., 2014). We find the effect of pressure on the velocities of FeO to be similar to that of MgO (Oganov and Dorogokupets, 2003) and MgO with moderate amounts of Fe (Wu et al., 2013).

3.3. Implications for ULVZs

Fig. 5 compares expected ULVZ velocities at the appropriate density with velocities of Fe bearing MgO compositions. The ULVZ values are obtained by adjusting PREM values at the CMB by the range of values generally reported for ULVZs. That is, V_p is reduced by 8% to 16% from PREM, V_s is reduced by 25% to 45% and density is increased by 5 to 15%. As can be seen in Fig. 5, we find that highly iron enriched MgO is able to match V_p and density of UL-VZs, but that V_s is not reduced enough. This is reflected in a compositionally dependent $(d\ln V_s/d\ln V_p)_{T,P}$ of 1.3–1.5 at PREM + 10% density, which is far lower than that the value of 3 generally observed in ULVZs. Slightly different values for $(d\ln V_s/d\ln V_p)_{T,P}$ can be obtained if we use a different temperature for the CMB but they are still far lower than those of ULVZs.

The conclusion that a highly Fe enriched MgO is not able to match all the properties of ULVZs is similar to the conclusion of Muir and Brodholt (2015) for Fe-enriched perovskite. In both phases, the reduction in V_s would require very high Fe concentrations ($\sim$100%) and thus would result in unreasonably high densities. However, we have not yet considered both phases simulta-
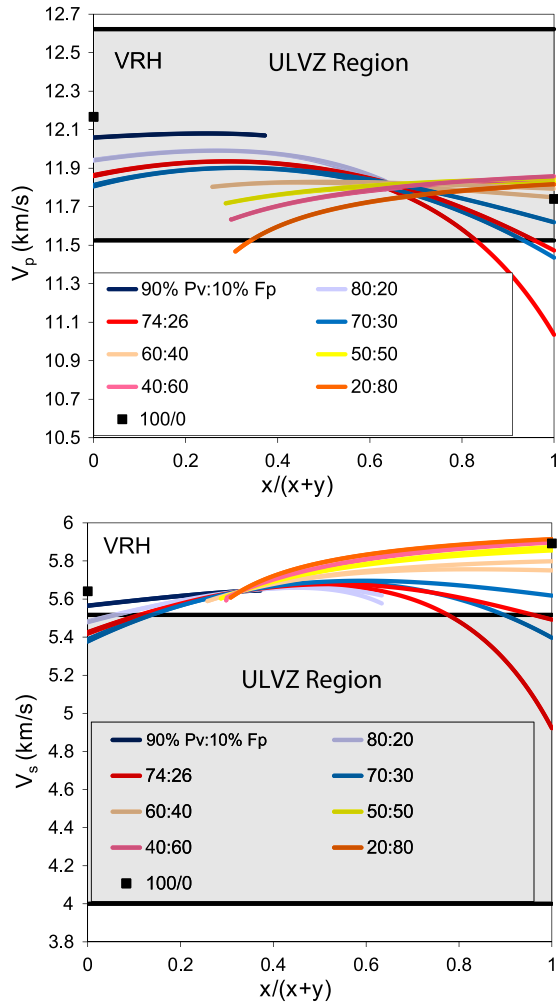
Fig. 6. Graph showing the velocities of various two phase mixtures of $Fe_xMg_{1-x}O$ and $Fe_yMg_{1-y}SiO_3$. Different volume fractions of the two phases (expressed as the pv volume%: fp volume%) are represented by different colours. The $x/(x + y)$ ratio (where $x + y = 1$) is varied from 0 (all iron in pv) to 1 (all iron in fp) and is given on the x-axis. x and y (the total amount of Fe in the system) are then set at each volume fraction and $x/(x + y)$ ratio so that the density is equal to PREM + 10%. The moduli are calculated with VRH bounds and the mixing bounds are HS. All volume fractions, therefore, have two bounds but these are only visible for some volume fractions ($74 : 26$ and $70 : 30$ for instance). (For interpretation of the references to color in this figure legend, the reader is referred to the web version of this article.)

neously. In order to do this there are three variables that can be adjusted: 1) the ratio of fp to pv, 2) the total amount of iron in the system, and 3) the partitioning of this iron between pv and fp. There are also two main sources of bounding error – firstly the individual pv and fp moduli have a value that is between the V and the R bounds and secondly a two phase mixture with unknown mixing geometry has HS bounds. If highly enriched fp is present the HS bounds are very large due to the very low G of FeO relative to perovskite.

Figs. 6 and 7 show the effect of iron partitioning on the properties of a two phase fp–pv system. The total amount of iron was fixed such that the density of the system matches the ULVZ density of PREM + 10%. The greatest reduction in velocities occurs when one phase or the other becomes strongly enriched in Fe, and so the lowest velocities for any particular mixture of phases is always achieved when 100% of the Fe is in the volumetrically smallest phase. The maximum iron enrichment is, however, restricted by the requirement to match ULVZ densities. For instance, with mantle-like phase proportions of 80% pv + 20% fp, only slight reductions in velocity occur if Fe is incorporated predominantly in
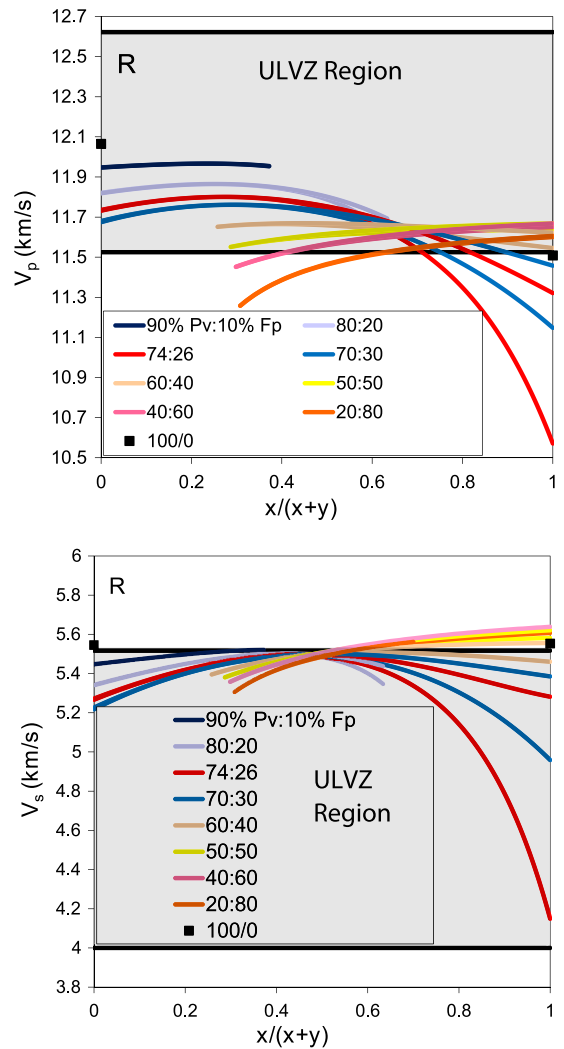
Fig. 7. Same as Fig. 6 but using Reuss averaging for the individual phases. (For interpretation of the references to color in this figure legend, the reader is referred to the web version of this article.)

perovskite. Stronger velocity reductions begin when Fe becomes more enriched in fp than pv but in this case the density increases beyond that of ULVZs (which is why the light blue line in Figs. 6 and 7 is truncated when the proportion of Fe in fp exceeds about 0.6). Alternatively, for a phase proportion of 20% pv + 80% fp, significant reductions in velocities only begin when most of the Fe is partitioned into the volumetrically minor phase pv but when pv becomes too enriched in Fe (above about 70%) the density again exceeds that of ULVZs. This is indicated in the figures by the truncation of the orange line at low values of Fe in pv.

The strongest reductions in velocities which satisfy the midpoint of the ULVZ density range are obtained for a phase proportion 74% pv + 26% fp and where all the Fe is partitioned into fp. This corresponds to a mixture of pure FeO and $MgSiO_3$. In this case, V_s drops by 25% to 43% depending upon the particular averaging scheme. As discussed earlier, $(d\ln V_s/d\ln V_p)_{T,P}$ for the individual phases is much smaller than the value of 3 observed in ULVZs but a much larger value can be obtained for a polyphase mixture of pv and fp with the exact value again depending on the particular averaging scheme used. For instance, using the Reuss averaged moduli $(d\ln V_s/d\ln V_p)_{T,P}$ for the individual phases and the HS bounds for the polyphase, $(d\ln V_s/d\ln V_p)_{T,P}$ can reach a maximum of 3.0. This increase is mostly due to the large range of possible velocities inside the HS bounds, however,
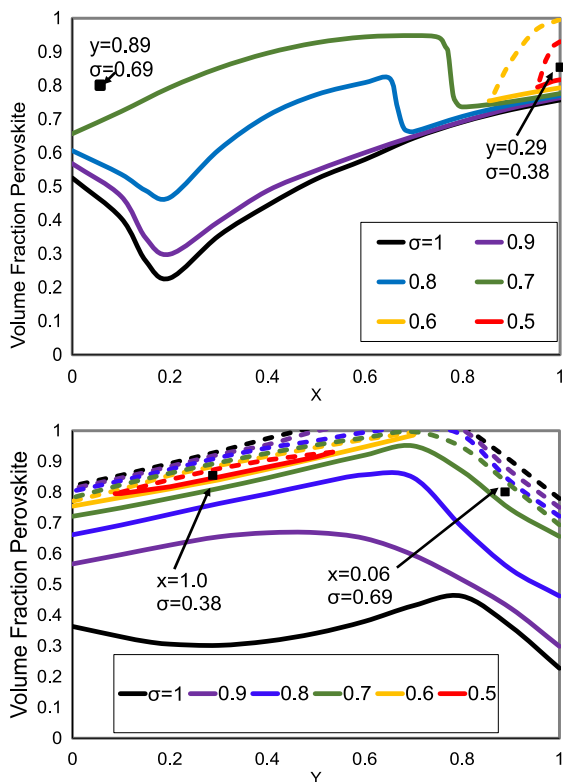
Fig. 8. Contour plot of the deviation from the middle of ULVZ property range for a two phase $Fe_xMg_{1-x}O$ and $Fe_{yy}Mg_{1-y}SiO_3$ mixture. σ is defined in Eq. (5) and is calculated for V_p, V_s and ρ and the reported σ is the highest of these three at any point. All solutions with $\sigma \leq 1$ have V_p, V_s and ρ that are within the range of ULVZs. The top figure (a) demonstrates the relationship between x and the fp:pv ratio and the lower figure (b) between y and the fp:pv ratio. The "best" solution of ULVZ properties is given by the square with $\sigma = 0.38$. Another local "best" solution with $\sigma = 0.69$ is also indicated. Values were constructed with Reuss bounds and the best fitting values within the HS bounds were chosen at each point. VRH and V bounds give worse fits. Solid lines are lower bounds, dashed lines are upper bounds for each σ value and for A most upper bounds would be above 1.

and the $(\mathrm{d}\ln V_s/\mathrm{d}\ln V_p)_{T,P}$ value taken from the middle of the HS bounds reaches a maximum of 2.1.

To further extend the comparison with ULVZs, we search for all two-phase mixtures of ferropericlase and perovskite that simultaneously produce V_p, V_s and density within the range of ULVZ values. For this we use the Reuss bounds as these produce the lowest velocities (Figs. 6 and 7). Fig. 8 shows the result of the search. All solutions above the solid line ($\sigma = 1$) and below the black dashed lines (only seen in Fig. 8b) fit all three ULVZ properties. Solutions outside this have at least one property outside the ULVZ range. As can be seen, there is a large range of ratios of fp to pv which are able to fit all three ULVZ observables. In order to give an indication of how well inside the range of ULVZ properties a particular solution lies, we have contoured the results in terms of σ as a measure of deviation from the middle of the ULVZ range. To do this we assume that ULVZs properties range from $\Delta\rho = 5–15\%$, $\Delta V_p = 8–15\%$ and $\Delta V_s = 24–45\%$ from the average PREM values. We then take the middle value of those ranges as the most likely ULVZ value ($\Delta\rho = 10\%$, $\Delta V_p = 13.5\%$ and $\Delta V_s = 34.5\%$) and half the range as an uncertainty ($\sigma(\Delta\rho) = \pm5\%$, $\sigma(\Delta V_p) = \pm3.5\%$) and $\sigma(\Delta V_s) = \pm10.5\%$). We then calculate the miss-fit of any possible ULVZ compositions from those middle values via Eq. (5):

$$\sigma^2 = \frac{(\Delta\rho_{model} - \Delta\rho_{ULVZ})^2}{(\Delta\rho_{ULVZ})^2} \qquad (5)$$

with an equivalent expression for V_p and V_s. In Fig. 8 we contour the maximum σ of all three variables. A $\sigma = 0$ would mean

that a solution produces V_p, V_s and density which match the exact middle of the ULVZ range. A $\sigma > 1$ would mean that at least one property is outside the ULVZ range. We realise that this is not a true measure of uncertainty or error, but it gives some indication of how securely a solution falls within the ULVZ range.

We can see in Fig. 8 that there is one "best" solution with $\sigma = 0.38$. This is approximately $0.85(Fe_{0.29}Mg_{0.71}SiO_3) + 0.15(FeO)$. There is another local best solution ($\sigma = 0.69$) where most iron partitions into pv and very little into fp. The "best" solution makes some sense in that strong partitioning of iron into ferropericlase is supported by experiments.

The partitioning of iron between ferropericlase and perovskite is affected by multiple factors. Increasing the total amount of iron or decreasing the pressure both act to decrease K_D (where K_D is the exchange coefficient and a low K_D indicates iron being partitioned into the fp phase), while increasing temperature increases K_D (Nakajima et al., 2012; Narygina et al., 2011; Sinmyo et al., 2008, 2011). Successive spin state transitions in ferropericlase and perovskite can cause K_D to decrease and then increase (Auzende et al., 2008; Irifune et al., 2010; Nakajima et al., 2012; Prescher et al., 2014; Sakai et al., 2009), and the presence of ferric iron, which in turn depends upon oxygen fugacity and the presence of aluminium, can cause an increase in K_D through its own spin transition (Nakajima et al., 2012; Prescher et al., 2014; Sinmyo and Hirose, 2013). In addition the conversion of perovskite to post-perovskite (Hirose, 2013) may decrease the concentration of iron in ferro-periclase (Auzende et al., 2008). In broad terms, however, while pyrolitic systems at lower mantle pressures and temperatures have a K_D of $\sim$0.4–0.9 (Irifune et al., 2010; Prescher et al., 2014; Sinmyo and Hirose, 2013), a mantle heavily enriched in ferrous iron would be expected to have a K_D of $<$0.1 (Nakajima et al., 2012). If ULVZs do have very high iron contents this would result in the strong partitioning of iron into ferro-periclase required to produce the observed ULVZs velocities and densities. The other local "best" solution has far too much Fe in perovskite relative to ferropericlase and we judge that to be an unlikely solution to ULVZs.

A considerable portion of the iron in the lower mantle can exist as ferric iron (Frost et al., 2004). Ferric iron in the A-site of pv will decrease both density and K (Catalli et al., 2010, 2011; Glazyrin et al., 2014). Lower densities will make it easier to fit ULVZ properties with a Fe-enriched mantle as it allows higher iron concentrations at ULVZ densities. On the other hand a lower K will impair fitting to ULVZ values as $V_s : V_p$ ratios will decrease further. These effects are small ($\sim$1%) and compensatory and will probably not overly affect fitting to ULVZs. On the other hand, ferric iron in the B site (either in Al-free pv or with an exchange between A-site Fe and B-site Al) has much larger effects due to its spin transition at $\sim$70 GPa (Catalli et al., 2010, 2011; Hsu et al., 2011). This spin transition increases k_D, as stated above, which will decrease the likelihood of highly enriched fp forming but it also increases K (which aids fitting to ULVZ properties) and density (which impairs fitting to ULVZ properties) on the order of $<$10% (Catalli et al., 2010, 2011). A playoff between these different effects means that the presence of ferric iron is likely to shift but not remove the possibility of fitting to ULVZs, but full calculation of the properties of ferric-bearing pv at lower mantle conditions is required to know the exact effect.

4. Conclusions

We find a strong decrease in seismic velocity upon addition of iron to MgO due to both the increased density and the decreased moduli. The effect of Fe increases with temperature due to the higher temperature dependence of the shear and bulk moduli of FeO relative to MgO. The bulk modulus is more sensitive

to the spin states of iron than the shear modulus which therefore affects V_p more than V_s. Above 25% Fe there is a significant discontinuity in K and V_p. We find that at ULVZ conditions shear wave velocities of FeO can become as low as 2.2 km/s. The highest value we can obtain for $(d\ln V_s/d\ln V_p)_{T,P}$ is 1.9 but that is for very high Fe contents which would increase the density above that observed in ULVZs. At ULVZ densities the highest value we obtain for $(d\ln V_s/d\ln V_p)_{T,P}$ is 1.5, making it hard to reconcile ULVZ observations with just (Mg, Fe)O.

While the shear velocities are too high in a single phase $Fe_xMg_{1-x}O$ system, we find that a mixture of perovskite and ferropericlase is able to simultaneously fit all measured ULVZ properties. In particular, small amounts of highly Fe-enriched periclase drop the shear velocities to well within the ULVZ range allowing appropriate V_s and V_p velocities at ULVZ densities. The choice of averaging for the moduli has a significant effect on mixing velocities, with Reuss and VRH averaging providing V_s values in the range of ULVZs. In addition the very low shear modulus of highly iron-enriched ferropericlase leads to large velocity bounds in polyphase systems. We also find that $(d\ln V_s/d\ln V_p)_{T,P}$ is significantly higher for the two-phase systems than for a single phase, and the highest possible value matches the expected ULVZ value of 3. We conclude, therefore, that a Fe-enriched lower mantle composition is able to explain the properties of ULVZs.

Acknowledgements

References

Auzende, A.-L., Badro, J., Ryerson, F.J., Weber, P., Fallon, S., Addad, A., Siebert, J., Fiquet, G., 2008. Element partitioning between magnesium silicate perovskite and ferropericlase: new insights into bulk lower-mantle geochemistry. Earth Planet. Sci. Lett. 269, 164–174.

Bower, D.J., Wicks, J.K., Gurnis, M., Jackson, J.M., 2011. A geodynamic and mineral physics model of a solid-state ultralow-velocity zone. Earth Planet. Sci. Lett. 303, 193–202.

Bucko, T., 2008. Ab-initio calculations of free-energy reaction barriers. J. Phys. Condens. Matter 20, 1–9.

Buffett, B.A., Garnero, E.J., Jeanloz, R., 2000. Sediments at the top of Earth's core. Science 290, 1338–1342.

Catalli, K., Shim, S.-H., Dera, P., Prakapenka, V.B., Zhao, J., Sturhahn, W., Chow, P., Xiao, Y., Cynn, H., Evans, W.J., 2011. Effects of the Fe^{3+} spin transition on the properties of aluminous perovskite – new insights for lower-mantle seismic heterogeneities. Earth Planet. Sci. Lett. 310, 293–302.

Catalli, K., Shim, S.-H., Prakapenka, V.B., Zhao, J., Sturhahn, W., Chow, P., Xiao, Y., Liu, H., Cynn, H., Evans, W.J., 2010. Spin state of ferric iron in $MgSiO_3$ perovskite and its effect on elastic properties. Earth Planet. Sci. Lett. 289, 68–75.

Chen, B., Jackson, J.M., Sturhahn, W., Zhang, D., Zhao, J., Wicks, J.K., Murphy, C.A., 2012. Spin crossover equation of state and sound velocities of $(Mg_{0.65}Fe_{0.35})$O ferropericlase to 140 GPa. J. Geophys. Res., Solid Earth 117, B082081 (9 pp.).

Davies, G.F., 1974. Effective elastic-moduli under hydrostatic stress 1. Quasi-harmonic theory. J. Phys. Chem. Solids 35, 1513–1520.

Dobson, D.P., Brodholt, J.P., 2005. Subducted banded iron formations as a source of ultralow-velocity zones at the core–mantle boundary. Nature 434, 371–374.

Dorfman, S.M., Duffy, T.S., 2014. Effect of Fe-enrichment on seismic properties of perovskite and post-perovskite in the deep lower mantle. Geophys. J. Int. 197, 910–919.

Frost, D.J., Liebske, C., Langenhorst, F., McCammon, C.A., Tronnes, R.G., Rubie, D.C., 2004. Experimental evidence for the existence of iron-rich metal in the Earth's lower mantle. Nature 428, 409–412.

Fukui, H., Tsuchiya, T., Baron, A., 2012. Lattice dynamics calculations for ferropericlase with internally consistent LDA + U method. J. Geophys. Res. 117, B122021 (10 pp.).

Garnero, E.J., Jeanloz, R., 2000. Fuzzy patches on the Earth's core-mantle boundary? Geophys. Res. Lett. 27, 2777–2780.

Glazyrin, K., Ballaran, T.B., Frost, D.J., McCammon, C., Kantor, A., Merlini, M., Hanfland, M., Dubrovinsky, L., 2014. Magnesium silicate perovskite and effect of iron

oxidation state on its bulk sound velocity at the conditions of the lower mantle. Earth Planet. Sci. Lett. 393, 182–186.

Hernlund, J.W., Jellinek, A.M., 2010. Dynamics and structure of a stirred partially molten ultralow-velocity zone. Earth Planet. Sci. Lett. 296, 1–8.

Hirose, K., 2013. High-pressure, high-temperature X-ray diffraction measurements and the discovery of post-perovskite phase transition. J. Phys. Soc. Jpn. 82.

Hsu, H., Blaha, P., Cococcioni, M., Wentzcovitch, R.M., 2011. Spin-state crossover and hyperfine interactions of ferric iron in $MgSiO_3$ perovskite. Phys. Rev. Lett. 106, 1185011 (4 pp.).

Hutko, A.R., Lay, T., Revenaugh, J., 2009. Localized double-array stacking analysis of PcP: D'' and ULVZ structure beneath the Cocos plate, Mexico, central Pacific, and north Pacific. Phys. Earth Planet. Inter. 173, 60–74.

Idehara, K., Yamada, A., Zhao, D., 2007. Seismological constraints on the ultralow velocity zones in the lowermost mantle from core-reflected waves. Phys. Earth Planet. Inter. 165, 25–46.

Irifune, T., Shinmei, T., McCammon, C., Miyajima, N., Rubie, D.C., Frost, D.J., 2010. Iron partitioning and density changes of pyrolite in Earth's lower mantle. Science 327, 193–195.

Isaak, D., Moser, S., 2013. Elasticity of single-crystal wustite at ambient and elevated temperature from resonant ultrasound spectroscopy. J. Phys. Chem. Solids 74, 879–885.

Jacobsen, S., Reichmann, H.J., Spetzler, H., Mackwell, S., Smyth, J., Angel, R., McCammon, C., 2002. Structure and elasticity of single-crystal (Mg, Fe)O and a new method of generating shear waves for gigahertz ultrasonic interferometry. J. Geophys. Res. 107 (4), 1–13.

Jensen, K., Thorne, M.S., Rost, S., 2013. SPdKS analysis of ultralow-velocity zones beneath the western Pacific. Geophys. Res. Lett. 40, 4574–4578.

Kanda, R.V.S., Stevenson, D.J., 2006. Suction mechanism for iron entrainment into the lower mantle. Geophys. Res. Lett. 33, L023101 (4 pp.).

Kono, Y.I.T., Higo, Y., Inoue, T., Barnhoorn, A., 2010. P–V–T relation of MgO derived by simultaneous elastic wave velocity and in situ X-ray measurements: a new pressure scale for the mantle transition. Phys. Earth Planet. Inter. 183, 196–211.

Kresse, G., Furthmuller, J., 1996. Efficient iterative schemes for ab initio total-energy calculations using a plane-wave basis set. Phys. Rev. B 54, 11169–11186.

Kresse, G., Joubert, D., 1999. From ultrasoft pseudopotentials to the projector augmented-wave method. Phys. Rev. B 59, 1758.

Labrosse, S., Hernlund, J.W., Coltice, N., 2007. A crystallizing dense magma ocean at the base of the Earth's mantle. Nature 450, 866–869.

Larico, R., Assali, L., Justo, J.F., 2013. Spin states of iron impurities in magnesium oxide under pressure: a possible intermediate state. Phys. Rev. B 87, 1651131 (8 pp.).

Lin, J.F., Gavriliuk, A., Struzhkin, V.V., Jacobsen, S., Sturhahn, W., Hu, M., Chow, P., Yoo, C.-S., 2007a. Pressure-induced electronic spin transition of iron in magnesiowustite-(Mg, Fe)O. Phys. Rev. B 73, 1131071 (4 pp.).

Lin, J.F., Speziale, S., Mao, Z., Marquardt, H., 2013. Effects of the electronic spin transitions of iron in lower mantle minerals: implications for deep mantle geophysics and geochemistry. Rev. Geophys. 51, 244–275.

Lin, J.F., Vanko, G., Jacobsen, S., Iota, V., Struzhkin, V.V., Prakapenka, V., Kuznetsov, A., Yoo, C.-S., 2007b. Spin transition zone in Earth's lower mantle. Science 317, 1740–1742.

Lu, L., Chen, Y., Chen, X.-R., Zhu, J., 2005. Thermodynamic properties of MgO under high pressure from first-principles calculations. Physica B 370, 236–242.

Manga, M., Jeanloz, R., 1996. Implications of a metal-bearing chemical boundary layer in D'' for mantle dynamics. Geophys. Res. Lett. 23, 3091–3094.

Mao, W.L., Mao, H.K., Sturhahn, W., Zhao, J.Y., Prakapenka, V.B., Meng, Y., Shu, J.F., Fei, Y.W., Hemley, R.J., 2006. Iron-rich post-perovskite and the origin of ultralow-velocity zones. Science 312, 564–565.

Muir, J., Brodholt, J., 2015. Elastic properties of ferrous bearing $MgSiO_3$ and their relevance to ULVZs. Geophys. J. Int. http://dx.doi.org/10.1093/gji/ggv045.

Nakajima, Y., Frost, D.J., Rubie, D.C., 2012. Ferrous iron partitioning between magnesium silicate perovskite and ferropericlase and the composition of perovskite in the Earth's lower mantle. J. Geophys. Res. 117, B082011 (12 pp.).

Narygina, O., Dubrovinsky, L., Samuel, H., McCammon, C., Kantor, I., Glazyrin, I., Pascarelli, S., Aquilanti, G., Prakapenka, V., 2011. Chemically homogeneous spin transition zone in Earth's lower mantle. Phys. Earth Planet. Inter. 185, 107–111.

Nomura, R., Ozawa, H., Tateno, S., Hirose, K., Hernlund, J., Muto, S., Ishii, H., Hiraoka, N., 2011. Spin crossover and iron-rich silicate melt in the Earth's deep mantle. Nature 473, 199–202.

Nose, S., 1984. A molecular-dynamics method for simulations in the canonical ensemble. Mol. Phys. 52, 255–268.

Oganov, A.R., Dorogokupets, P.I., 2003. All-electron and pseudopotential study of MgO: equation of state, anharmonicity, and stability. Phys. Rev. B 67, 2241101.

Ozawa, H., Hirose, K., Tateno, S., Sata, N., Ohishi, Y., 2010. Phase transition boundary between B1 and B8 structures of FeO up to 210 GPa. Phys. Earth Planet. Inter. 179, 157–163.

Perdew, J.P., Ruzsinszky, A., Csonka, G.I., Vydrov, O.A., Scuseria, G.E., Constantin, L.A., Zhou, X.L., Burke, K., 2008. Restoring the density-gradient expansion for exchange in solids and surfaces. Phys. Rev. Lett. 100, 1364061 (4 pp.).

Persson, K., Bengtson, A., Ceder, G., Morgan, D., 2006. Ab-initio study of the composition dependence of the pressure-induced spin transition in the (Mg_{1-x}, Fe_x)O system. Geophys. Res. Lett. 33, L163061 (5 pp.).

Petford, N., Yuen, D., Rushmer, T., Brodholt, J., Stackhouse, S., 2005. Shear-induced material transfer across the core-mantle boundary aided by the post-perovskite phase transition. Earth Planets Space 57, 459–464.

Prescher, C., Langenhorst, F., Dubrovinsky, L., Prakapenka, V., Miyajima, N., 2014. The effect of Fe spin crossovers on its partitioning behavior and oxidation state in a pyrolitic Earth's lower mantle system. Earth Planet. Sci. Lett. 399, 86–91.

Reichmann, H.J., Jacobsen, S., Mackwell, S., McCammon, C., 2000. Sound wave velocities and elastic constants for magnesiowustite using Gigahertz interferometry. Geophys. Res. Lett. 27, 799–802.

Rondenay, S., Cormier, V.F., Van Ark, E.M., 2010. SKS and SPdKS sensitivity to two-dimensional ultralow-velocity zones. J. Geophys. Res., Solid Earth 115, B043111 (17 pp.).

Sakai, T., Ohtani, E., Terasaki, H., Sawada, N., Kobayashi, Y., Miyahara, M., Nishijima, M., Hirao, N., Ohishi, Y., Kikegawa, T., 2009. Fe–Mg partitioning between perovskite and ferropericlase in the lower mantle. Am. Mineral. 94, 921–925.

Scanavino, I., Belousov, R., Prencipe, M., 2012. Ab initio quantum-mechanical study of the effects of the inclusion of iron on thermoelastic and thermodynamic properties of periclase (MgO). Phys. Chem. Miner. 39, 649–663.

Scanavino, I., Prencipe, M., 2013. Ab-initio determination of high-pressure and high-temperature thermoelastic and thermodynamic properties of low-spin $(Mg_{1-x}Fe_x)O$ ferropericlase with x in the range [0.06, 0.59]. Am. Mineral. 98, 1270–1278.

Sinmyo, R., Glazyrin, I., McCammon, C., Kupenko, I., Kantor, A., Potapkin, V., Ruffer, R., Dubrovinsky, L., 2014. The influence of solid solution on elastic wave velocity determination in (Mg, Fe)O using nuclear inelastic scattering. Phys. Earth Planet. Inter. 229, 16–23.

Sinmyo, R., Hirose, K., 2013. Iron partitioning in pyrolitic lower mantle. Phys. Chem. Miner. 40, 107–113.

Sinmyo, R., Hirose, K., Muto, S., Ohishi, Y., Yasuhara, A., 2011. The valence state and partitioning of iron in the Earth's lowermost mantle. J. Geophys. Res., Solid Earth 116.

Sinmyo, R., Hirose, K., Nishio-Hamane, D., Seto, Y., Fujino, K., Sata, N., Ohishi, Y., 2008. Partitioning of iron between perovskite/postperovskite and ferropericlase in the lower mantle. J. Geophys. Res., Solid Earth 113, B112041 (11 pp.).

Speziale, S., Milner, A., Lee, V.E., Clark, S.M., Pasternak, M.P., Jeanloz, R., 2005. Iron spin transition in Earth's mantle. Proc. Natl. Acad. Sci. USA 102, 17918–17922.

Stackhouse, S., Brodholt, J.P., Price, G.D., 2007. Electronic spin transitions in iron-bearing $MgSiO_3$ perovskite. Earth Planet. Sci. Lett. 253, 282–290.

Thomas, C., Liu, Q., Agee, C., Asimow, P.D., Lange, R., 2012. Multi-technique equation of state for Fe_2SiO_4 melt and the density of Fe-bearing silicate melts from 0 to 161 GPa. J. Geophys. Res. 117, B102061 (18 pp.).

Thorne, M.S., Garnero, E.J., Jahnke, G., Igel, H., McNamara, A.K., 2013. Mega ultra low velocity zone and mantle flow. Earth Planet. Sci. Lett. 364, 59–67.

Wentzcovitch, R., Justo, J.F., Wu, Z., da Silva, C.R.S., Yuen, D., Kohlstedt, D., 2009. Anomalous compressibility of ferropericlase throughout the iron spin cross-over. Proc. the Natl. Acad. Sci. 106, 8447–8452.

Wicks, J.K., Jackson, A., Sturhahn, W., 2010. Very low sound velocities in iron-rich (Mg, Fe)O: implications for the core–mantle boundary region. Geophys. Res. Lett. 37, L153041 (5 pp.).

Wu, Z., Justo, J.F., da Silva, C.R.S., de Gironcoli, S., Wentzcovitch, R., 2009. Anomalous thermodynamic properties in ferropericlase throughout its spin crossover. Phys. Rev. B 80, 0144091 (8 pp.).

Wu, Z., Justo, J.F., Wentzcovitch, R., 2013. Elastic anomalies in a spin-crossover system: ferropericlase at lower mantle conditions. Phys. Rev. Lett. 110, 2285011 (5 pp.).

Wu, Z., Wentzcovitch, R., 2014. Spin crossover in ferropericlase and velocity heterogeneities in the lower mantle. Proc. Natl. Acad. Sci. USA 111, 10468–10472.